CHEMISTRY OF MATERIALS

pubs.acs.org/cm

Article

Facile Synthesis of Oxyhydrides by Reaction with $NaBH_4$ in an Open System

Published as part of Chemistry of Materials special issue "Honoring the Outstanding Scientific Contributions of Clare Grey".

Megan E. Burrill, Islamiyat Ojelade, Erica Truong, Tomas Orlando, Rongfu Zhang, Yan-Yan Hu, James M. Rondinelli, and Sossina M. Haile*

Cite This: *Chem. Mater.* 2026, 38, 4961−4974

Read Online

ACCESS | Metrics & More | Article Recommendations | Supporting Information

ABSTRACT: Oxyhydrides are an intriguing class of materials in which there is partial replacement of the oxide ion with hydride ions and oxygen vacancies. Conventional synthesis relies on vacuum sealed ampules, using long reaction times at high temperatures, limiting accessibility. Here, we demonstrate a rapid, ambient-pressure route to oxyhydride formation using $NaBH_4$ under flowing argon in just 1 h. This approach significantly lowers experimental barriers, enabling broader exploration of these materials. The maximum hydride incorporation, obtained using a reaction temperature of 400 °C, is given by the formula $SrTiO_{2.945}H_{0.049}$, where the hydride, oxygen vacancy, and unpaired electron concentrations are determined through thermogravimetric analysis, quantitative solid-state nuclear magnetic resonance spectroscopy (NMR), and electron paramagnetic resonance spectroscopy. Density functional theory simulations of the ^{1}H NMR shifts for candidate point defects support the assignment of the observed hydride peak, validating the efficacy of the synthetic approach. A combination of *in situ* and *ex situ* studies of the reaction pathway reveal that hydride incorporation into the perovskite occurs *via* direct solid−solid reaction, with higher reaction temperatures favoring $NaBH_4$ decomposition and H_2(g) release over oxyhydride formation. The electronic defect structure established from the EPR and NMR studies indicate that, at ambient temperature, anion vacant sites are occupied by single electrons, whereas hydride sites do not trap electrons. This work establishes a scalable synthesis strategy and provides a computational-experimental framework for understanding defect chemistry in oxyhydrides, opening pathways for their integration into energy and electronic applications.

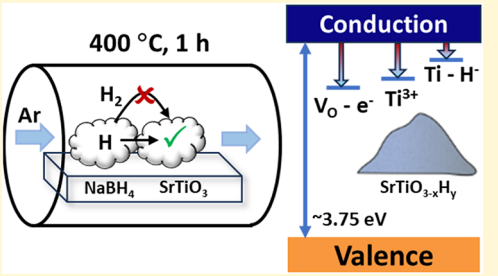

INTRODUCTION

In oxyhydride perovskites, hydrogen has a negative oxidation state and partially occupies the anion site, making for an uncommon heteroanionic system. In these materials, the anion site features a mix of oxide ions, hydride ions, and vacancies. Within this class, titanate perovskite oxyhydrides $ATiO_{3-x}:H_y$ (A = Ca, Sr, and Ba, denoted as ATO:H- in this paper) have received considerable attention.[1−3] Overall charge balance in the presence of the positively charged defects on the anion site is achieved by introduction of excess electrons into the system, effectively reducing Ti^{4+} to a slightly lower oxidation state.[4−6] Tunable defect concentrations suggest tunable properties. However, control and quantification of the anion site chemistry has been difficult to achieve, with many, though not all, authors taking oxygen deficiency to be directly equal to hydride content ($x = y$).[7−10] Thus, the underlying factors that govern the properties that emerge from the anion chemistry remain somewhat opaque. These challenges have impeded efforts to control properties for desired functionality.

Perovskite oxyhydrides are most commonly synthesized by reacting the relevant precursor oxide with CaH_2 in a vacuum-sealed ampule at temperatures of 500−600 °C for up to a week.[1,4−15] The process requires extreme care as CaH_2 is pyrophoric, and hydrogen gas evolved during the reaction can cause the ampule in which the reactants are sealed to explode.[16,17] Furthermore, removal of the byproduct CaO and unreacted CaH_2 from the desired perovskite phase can be challenging. Reaction with $NaBH_4$ provides an intriguing alternative to reaction with CaH_2, as the former is relatively safe for handling and the expected byproducts, NaOH, B_2O_3 and $NaBO_2$, along with any unreacted $NaBH_4$, are soluble (or decompose into soluble components) in water. Moreover, the ready thermal decomposition of $NaBH_4$ results in a relatively high equilibrium hydrogen pressure at moderate temperatures, reaching 1 atm at ∼530 °C.[18] This property creates the

Received: November 25, 2025
Revised: May 1, 2026
Accepted: May 7, 2026
Published: May 13, 2026

possibility of using $NaBH_4$ to generate oxyhydrides in an open rather than sealed chamber because high hydrogen pressure can be locally generated at temperatures low enough to favor hydride incorporation into the solid. At high reaction temperatures, oxyhydride formation is in competition with simple release of oxygen (*i.e.*, vacancy creation), even in a closed reaction vessel, and hydride incorporation may be precluded.

While $NaBH_4$ is an atypical reagent for oxyhydride synthesis, Nedumkandathil et al. have reported a comparative study of a series of hydride reagents, including $NaBH_4$, using the conventional sealed ampule approach for the preparation of BTO:H-.[7] These authors found $NaBH_4$ to be more effective at removing oxygen from the host perovskite than CaH_2, but that it ultimately generated a lower concentration of hydride than other hydride reagents. Leveraging the reducing power of $NaBH_4$, Tan et al.[19] reacted $SrTiO_3$ (STO) with $NaBH_4$ at moderate temperatures (300−375 °C) under flowing Ar and obtained a visibly darkened product in just 30−60 min. The authors, who were focused on the photocatalytic properties of the resulting material, made the plausible assumption that the oxide was simply reduced, without consideration of possible hydride incorporation.

In the present work, we evaluate the feasibility of STO:H- formation by the relatively straightforward reaction of STO and $NaBH_4$ under flowing Ar. Through a variety of experimental and computational methods, including thermogravimetric analysis (TGA), nuclear magnetic resonance (NMR) spectroscopy, electron paramagnetic resonance (EPR) spectroscopy, and density functional theory (DFT) simulations, we demonstrate that this reaction not only reduces the STO, but also results in hydride uptake. From these comprehensive studies, we assess the nature of the electronic defects in the STO:H- generated by this synthesis approach. We further elucidate aspects of the reaction pathway *via* selected *in situ* studies. Under the most favorable conditions, the hydride content is comparable to that reported by Nedumkandathil et al. for the reaction of $BaTiO_3$ with $NaBH_4$ in a sealed ampule at 600 °C for 2 days.[7] While the hydrogen concentration is lower than obtained from reaction of $SrTiO_3$ with CaH_2 (again in sealed ampules using higher temperatures and longer times[8,10,14]), the accessibility of this synthetic approach may enable a wider study of oxyhydride materials.

METHODS

Synthesis

Pristine STO powder was synthesized using solid state reaction of TiO_2 (Sigma-Aldrich 13463−67−7, lot SZB90340 V) and $SrCO_3$ (Sigma-Aldrich 7440−26−6, lot MKBC2844 V); after rotary ball milling in ethanol for 24 h, the powder was dried, pressed into a 32 mm pellet, then calcined for 10 h at 1100 °C in static air with heating and cooling ramp rates of 3 °C per minute. X-ray diffraction (XRD) confirms formation of a phase-pure cubic perovskite, Figure S3a. After calcination, the powder was ground in an agate mortar and pestle, then sieved through a 75 μm mesh to reject large agglomerates. The powder was heat-treated overnight in a 130 °C oven, then immediately transferred to an argon glovebox. There it was combined with $NaBH_4$ (Aldrich 452882, lot SHBJ2594) in a 1:1 molar ratio and ground for 30 min using an agate mortar and pestle. The mixture, with a total mass of ∼1 g for each reaction, was lightly pressed into an alumina crucible, removed from the glovebox, and quickly loaded into a horizontal tube furnace that was open to air. The furnace was purged with Ar gas (150 mL/min) for 2 h at room temperature to remove residual gases prior to heating to the reaction temperature (T_{rxn}).

The targeted reaction is represented as

$$SrTiO_3(s) + xNaBH_4(s) \rightarrow SrTiO_{3-3x}H_{2x}(s) + xNaBO_2(s) + xH_2O(g) \quad (1)$$

Although several sodium borate compounds are known, and thus are possible byproducts, this reaction captures the essence of the synthesis approach.

Each synthesis reaction consisted of a 1 h dwell at T_{rxn} between 350 and 425 °C under an Ar flow of 150 mL/min, supplied to remove the product H_2O. The temperature ramp rate was 6.33 °C/min (corresponding to a 1 h ramp for the 400 °C reaction condition). After reaction, the powder mixture was typically dark gray, however some individual particles, toward the inlet side of the tube, were white, indicating they had been oxidized. It was not possible to exclude these particles, which constituted a very small fraction of the total volume, from the analyzed material. Once removed from the furnace, the powders were sonicated for 30 min in deionized and degassed water, where degassing consisted of bringing the water to a boil for several minutes then quickly cooling to ambient temperature. In the absence of this degassing step, the product was typically contaminated with carbonates, where the CO_2 presumably originated from the water. The sample produced from reaction at 425 °C was washed with ethanol rather than water due to significant sparking when such samples were first contacted with water. The powders were collected by filtering the solution and then dried in an 80 °C oven. Though impurity phases were generally not detected by standard X-ray powder diffraction, elimination of surface adsorbates *via* degassing the water used for washing and drying the powder was necessary to obtain meaningful TGA and NMR measurements. Scanning electron microscopy (SEM) imaging revealed that the primary particle size of the oxide following solid state synthesis was ∼150−200 nm, and that the particle morphology was unchanged by the reaction to form the oxyhydride (Figure S13).

Oxyhydride powders in the as-synthesized condition were characterized with XRD and TGA. Prior to NMR experiments, the powders, including pristine STO, were further dried overnight under flowing 10% H_2/Ar gas at 200 °C and then stored in an Ar glovebox. The possibility that an amorphous, boron-containing impurity may have been overlooked in the XRD analysis of as-synthesized materials was evaluated by subjecting the samples to a 4 h heat treatment at 900 °C (3 °C/min ramp up, 4 °C/min ramp down) under static air. This treatment was intended to crystallize any such impurities, which would then be detected in subsequent diffraction measurements.[7]

Building on our observation that 400 °C reaction yields the highest hydride incorporation, we conducted a series of additional synthesis experiments at this temperature to probe the underlying reaction mechanism: one in which the dwell time was increased to 2 h, while holding the STO:$NaBH_4$ molar ratio at 1:1; one in which the molar ratio was changed to 1:0.5, while holding the reaction time to 1 h; and one in which the gas was changed to hydrogen (150 mL/min), with other reaction conditions unchanged. To facilitate characterization of bulk hydride species, free from contributions of surface species, samples were also prepared using $NaBD_4$ (Sigma-Aldrich 205591, lot MKCV9090) as the reactant. The default 400 °C reaction condition was employed, with all other steps identical to reaction with $NaBH_4$, including washing with degassed H_2O. These steps ensure that the bulk species are deuterium, while any surface species are related to hydrogen. The full set of synthesis experiments are described in Table S1. Based on the success of the reaction, we performed additional preliminary studies using this approach on other perovskite titanates. As with strontium titanate, each of the reactants underwent a color change following the treatment, as depicted in Figure S15, suggesting the generalizability of this approach.

The reaction pathway was further probed by several methods. These included monitoring the composition of the reaction exhaust gas, simultaneous thermal analysis of the reaction as it occurred, and

https://doi.org/10.1021/acs.chemmater.5c03181
Chem. Mater. 2026, 38, 4961−4974

in situ X-ray powder diffraction as described below. The experimental details of these *in situ* measurements are provided in Tables S3−S4.

CHARACTERIZATION

Powder X-ray Diffraction

Powder diffraction with a copper source Rigaku Ultima IV and a 30 μm thick Ni-filter was used to establish phase formation and measure lattice parameter. The as-synthesized powders were measured using a scan speed of 2.5° min^{-1} and a scan step size of 0.04° in 2θ. After subjecting the powders to the additional 900 °C heat treatment, diffraction data were collected using the same instrument and scan speed and step size of 1.5° min^{-1} and 0.04° in 2θ, respectively. Structure refinements were performed using the GSAS-II program.[20]

Solid-State NMR Spectroscopy

^{1}H and ^{11}B magic-angle-spinning (MAS) NMR experiments were performed on a Bruker Avance III-HD 400-MHz spectrometer. Details of the ^{11}B measurements are described in the SI. Samples for ^{1}H characterization were packed in an Ar-glovebox into a 4 mm zirconia rotor and transferred to the NMR spectrometer in a vacuum chamber. For all ^{1}H experiments, a spin−echo pulse sequence was used with a $\pi/2$ pulse length of 2.4 μs. Data were collected at a MAS speed of 12.5 kHz and calibrated to adamantane (Sigma-Aldrich, 100277, CAS 281−23−2) at 1.83 ppm relative to tetramethyl silane. Qualitative 1-D NMR spectra were obtained by measuring 320 scans with a recycle delay time of 25 s, except for the sample fabricated under H_2, which required a delay time of 35 s for full relaxation. For quantitative NMR determination of hydrogen content, ∼1.5 mg of adamantane standard (Aldrich 100277−25g, lot MKCK0000) was mixed with ∼170 mg of sample in air and loaded into the rotor and 16 scans were collected. The delay time was 20 s for the samples fabricated at 363−387 °C and 15 s for the sample fabricated at 400 °C, in all cases longer than five times the longest T_1 relaxation of the hydride signal. Fitting of the spectra to obtain the integrated intensities was completed in DMFit; uncertainties were determined using the built in Monte Carlo error estimation tool;[21] two standard deviations were used for computing the compositional uncertainties. Spin−lattice relaxation times, T_1, were measured using a spin−echo, saturation-recovery pulse sequence; the recovery delay times were chosen to ensure full relaxation to equilibrium magnetization. For each recovery time, 16 scans were acquired.

^{2}H MAS NMR data were collected on a Bruker Avance III-HD 800-MHz 63 mm bore spectrometer. A single-pulse experiment was used with a delay time of 100 s, $\pi/2$ pulse length of 3.8 μs, and 1024 scans. The sample was packed under air into a 3.2 mm pencil rotor and spun at a MAS speed of 15 kHz. D_2O at 0 ppm was used as the reference. Fitting was completed in ssNake using the Quadrupolar model.[22]

Electron Paramagnetic Resonance (EPR)

Approximately 78 mg of the sample was packed into a 4 mm thick-wall screw-cap quartz EPR tube. Continuous-wave electron paramagnetic resonance (CW-EPR) measurements were performed on a Bruker E580 spectrometer operating at 9.3 GHz and equipped with an Oxford ESR900 flow cryostat. The spectra were recorded at 10 K using a modulation amplitude of 1 G and a modulation frequency of 100 kHz.

The absorptive spectrum was obtained using Easyspin software by numerical integration of the first-derivative spectrum after baseline correction. The resulting absorption spectra were then double-integrated to obtain the signal intensity, which was normalized to the sample mass for comparison.

Thermogravimetric Analysis (TGA)

Following a procedure demonstrated by Nedumkandathil [7], total anion-site nonstoichiometry was determined from mass uptake during reoxidation using a Netzsch simultaneous thermal analyzer (STA) 449C. Samples, ∼180 mg in mass, were placed in an alumina crucible and the gas flow conditions set to 100 mL/min synthetic air as the purge gas and 30 mL/min Ar as the protective gas. A buoyancy correction measurement was performed using a similar mass of fused alumina and identical data collection parameters. Mass was recorded upon heating the samples at a rate of a 2 °C/min ramp and holding for 2 h at 580 °C. In some cases, evolved gases were analyzed using an inline mass spectrometer (Pfeiffer GSD320). Uncertainty in the TGA analysis was determined using the fluctuations in high and low bounds of the final mass due to noise in the signal.

Reaction Pathway Characterization

To capture the full reaction products from a synthesis at 425 °C, a sample prepared at this temperature in the standard tube furnace (with all other reaction conditions held at the default values) was examined without applying the washing step. Following the completion of the reaction, the sample was quickly transferred into the glovebox and loaded into a Rigaku airtight sample holder. The XRD pattern was measured in a Rigaku Generation 2 Smartlab with a copper source and a 30 μm thick Ni-filter utilizing a scan speed of 1.5 ° min^{-1} and a scan step size of 0.02 ° in 2θ.

In situ diffraction experiments to directly monitor the reaction as it progressed were performed using a Rigaku Generation 3 Smartlab equipped with an Anton Paar HTK 1200 M furnace, a molybdenum source, and a 15 μm thick Zr-filter. Reactions were performed at 400 °C and at 425 °C for a dwell time of ∼1.25 h. The sample mass was ∼0.2 g (with the default 1:1 molar ratio of precursors). The Ar gas flow (210 mL/min) was directed downward through the sample, which in turn, was placed on a fine mesh. The gas flow geometry is somewhat different from the configuration in the horizontal tube furnace employed for preparing samples but, nevertheless, provides valuable insight into the progress of the reaction. So as to mimic the synthesis procedure, diffraction patterns were collected continuously, while the heating progressed. The data collection period for each pattern (outside of the initial and final patterns) was 13 min, corresponding to about an 80 °C difference in temperature between the first and final positions in the pattern. Scan speeds and angular range are detailed in Tables S3−S4. The *in situ* TGA/DSC measurement utilized a Netzsch simultaneous thermal analyzer (STA) 509 Select. The 28.3 mg sample (comprised of a 1:1 molar ratio of the two precursors) was placed into an alumina crucible with no lid. The measurement consisted of the usual, 1 h ramp to 400 °C, followed by a 2 h dwell (twice as long as the usual condition) at the reaction temperature. Total gas flow was 150 mL/min Ar. The buoyancy correction measurement used empty alumina crucibles. Though the vertical gas flow in the STA is again different from that of the horizontal tube furnace, the measurements provide valuable information regarding the occurrence of thermal events. An identical reaction (1 h ramp to 400 °C, 2 h dwell, 1:1 molar ratio with $NaBD_4$, all other

https://doi.org/10.1021/acs.chemmater.5c03181
Chem. Mater. 2026, 38, 4961−4974

reaction conditions at default values) in the tube furnace was directly monitored *via* direction of the exhaust gas to an inline mass spectrometer (Pfeiffer Thermostar).

COMPUTATIONAL METHODS

Density Functional Theory (DFT): Defect Structure Simulation

Density functional theory (DFT) relaxation calculations were performed using the Vienna Ab initio Simulation Package (VASP).[23−25] All simulations employed projector augmented wave (PAW) pseudopotentials with the PBE-GGA exchange−correlation functional,[26,27] a plane-wave cutoff energy of 600 eV, and a Γ-centered 4 × 4 × 4 *k*-point grid. Electron configurations in the PAW potentials were H ($1s^1$), O ($2s^2\ 2p^4$), Ti ($3s^2\ 3p^6\ 3d^3\ 4s^1$), and Sr ($4s^2\ 4p^6\ 4d^{0.001}\ 5s^{1.999}$). Spin-polarized calculations with an initial magnetic moment of 1 μ_B were applied for defect relaxations. A full relaxation of the pristine $SrTiO_3$ (STO) unit cell was carried out first, and the resulting lattice parameters were used for defect-containing cells, where only atomic positions were relaxed. This choice was justified by comparing the dimensions of relaxed cells, with and without the substitutional hydride defect. The difference in volume was found to be less than 0.5%, validating the use of partial relaxation of the defect cells. Each defect was considered in isolation (*i.e.*, dilute limit approximation), matching the experimental observation of a low hydrogen concentration.

Although hydrogen incorporation in perovskite oxyhydrides is typically assumed to occur at an oxygen site forming the substitutional hydride defect, alternative incorporation sites are possible.[28] Several representative configurations considered in this work are illustrated in Figure 1, where Kröger−Vink notation is used to denote the character of the defects.[29] NMR spectroscopy in combination with computational simulation of the peak positions of possible defects affords a means of assessing the prevalence of alternative defects. Considered here, in addition to the substitutional hydride defect ($H_O^\bullet$), are the interstitial proton ($H_i^\bullet$), the complex formed between a Sr-vacancy and one ($(V_{Sr}-H)'$) or two ($(V_{Sr}-2H)^x$) protons, the complex formed between a Sr-vacancy and a trapped H_2 molecule ($(V_{Sr}-H_2)''$), and the complex formed between a Ti-vacancy and one ($(V_{Ti}-H)'''$) or two ($(V_{Ti}-2H)''$) protons. Note that the interstitial proton is equivalently defined as the hydroxyl defect residing on an oxygen site, $OH_O^\bullet$, whereas $(V_{Sr}-2H)^\times$ and $(V_{Sr}-H_2)''$, with differing charge states, are distinct. These defects are selected on the basis of the computational study by Varley et al. that demonstrated these to be the most energetically favorable configurations for hydrogen incorporation.[28]

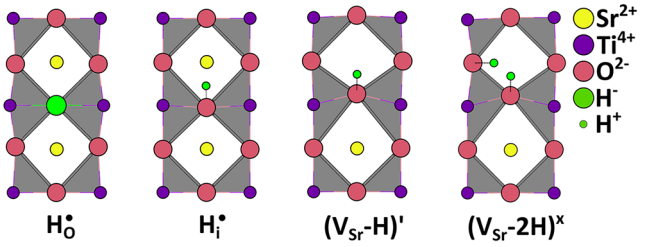

Figure 1. Schematic representation of point defects as predicted by DFT simulations; local distortions are exaggerated to enhance visual clarity.

In order to assess the NMR response of a representative surface species, simulations of a single configuration of adsorbed surface hydroxide, selected from previous work,[30] were also performed. Surface OH groups were modeled using the "2 × 1-DissA" structure reported by Becerra-Toledo.[30] The slab model employed a converged *z*-axis of 40 Å, providing approximately 10 Å of vacuum to eliminate spurious interactions between periodic images. These parameters ensure reliable modeling of defect energetics and local structural distortions associated with hydride incorporation.

Density Functional Theory: NMR and EFG Simulations

^{1}H NMR shifts were simulated in Quantum Espresso (QE) using the gauge including projector augmented wave (GIPAW) extension.[31,32] The following PAW norm-conserving pseudopotentials were employed: H.pbe-tm-new-gipaw-dc.UPF ($1s^1$), O.pbe-tm-new-gipawdc.UPF ($2s^2\ 2p^4$), Sr.pbe-tm-gipaw-dc.UPF ($4d^0\ 5s^1\ 4d^0\ 6s^0\ 6p^0\ 5d^0$), and Ti.pbe-tm-gipawsemi-dc.UPF ($3s^2\ 3p^6\ 3d^2$) from Ceresoli.[33,34] A cutoff energy of 950 eV and a Γ-centered 4 × 4 × 4 *k*-point grid were used to obtain the hydrogen defect properties. Calculated isotropic magnetic shielding (σ_{iso}) were converted to isotropic chemical shifts (δ_{iso}) using reference compounds as described in Figure S1. As noted, ATO:H- oxyhydrides become increasingly metallic as the hydride loading increases. In the NMR spectrum, this is expected to induce a Knight shift.[6,35] This effect cannot be calculated in pseudopotential based-DFT methods, and comparisons to experiment are thus qualitative.

^{2}H EFG simulations were completed in QE using the GIPAW extension and the same pseudopotentials as utilized for the ^{1}H NMR shift simulations. A cutoff energy of 950 eV, a Γ-centered 6 × 6 × 6 *k*-point grid, and quadrupolar moments from the 2008 tables[36] were used to obtain the EFG tensor for the ^{2}H defects. The relationship between Ti−H−Ti bond length and value of the quadrupolar

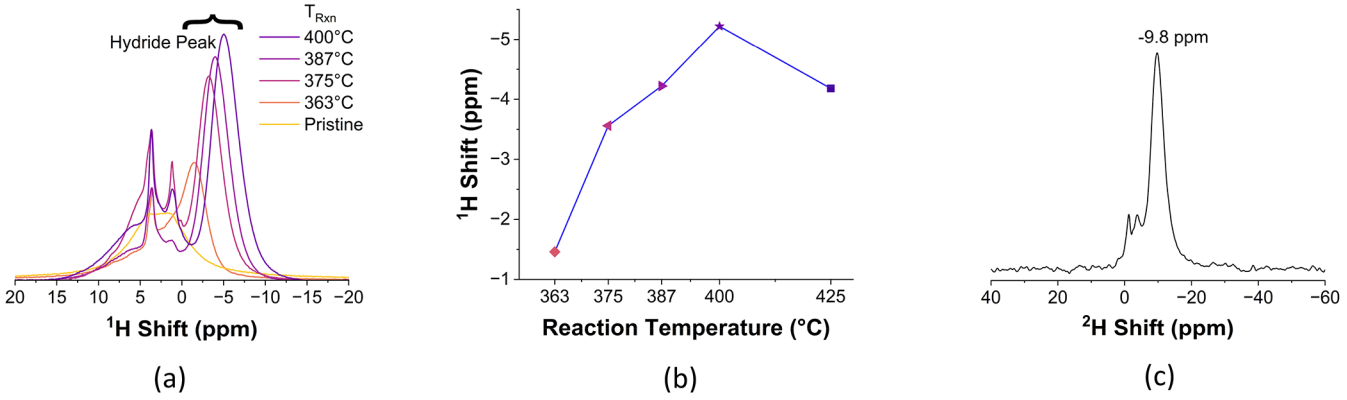

Figure 2. MAS NMR spectra of the products of the reaction of $SrTiO_3$ and $NaBH_4$/$NaBD_4$: (a) ^{1}H spectra collected at an MAS rate of 12.5 kHz for products generated from reaction with $NaBH_4$ at the temperatures indicated, along with that of pristine $SrTiO_3$, showing the strong influence of reaction temperature; (b) trend between the ^{1}H shift and the reaction temperature; and (c) ^{2}H spectrum collected at 15 kHz MAS for a sample reacted with $NaBD_4$ at 400 °C, showing the presence of a single dominant resonance. The full ^{2}H spectrum, including SSBs, is shown in Figure S8.

https://doi.org/10.1021/acs.chemmater.5c03181
Chem. Mater. 2026, 38, 4961−4974

Table 1. Computed NMR Shifts for Various Defects Stable in Reducing Environments and Surface Hydroxide Groups

species	$H_O^{\bullet}$	$H_i^{\bullet}$	$(V_{Sr}-H)'$	$(V_{Sr}-H_2)''$	$(V_{Sr}-2H)^x$	$(V_{Ti}-H)'''$	$(V_{Ti}-2H)''$	surface OH
Calculated shift (ppm)	−1.0	−0.1	0.3	1.2, 1.3	1.4, 1.4	1.6	1.3, 2.1	4.5, 5.5

coupling constant, C_Q, was explored by varying the Ti−H−Ti bond length from 3.8802 to 4.2886 Å.

RESULTS AND DISCUSSION

XRD and NMR Evidence of Hydride Incorporation

XRD analysis shows that the average perovskite structure of STO, while remaining cubic (Figure S3), expands following reaction with $NaBH_4$. The cell parameter increases with reaction temperature, reaching a maximum value of about 3.9075 Å, Figure S3b. This slight increase in volume is consistent with the full cell relaxation from DFT. While these crystallographic changes indicate that reduction occurs, they are inconclusive with respect to hydride uptake. In contrast, clear evidence for hydride uptake is provided by the NMR data. The ^{1}H NMR spectra, Figure 2a, display a dominant peak in the shift range between 0 and −6 ppm, the magnitude and position of which vary systematically with reaction temperature. The maximum magnitude of this shift is reached at a reaction temperature of 400 °C (Figure 2b), beyond which both the shift and the magnitude of this peak decline (see Figure S6a for the complete set of spectra; for visual clarity, the 425 and 350 °C spectra are omitted from Figure 2a). This peak, which lies at a shift significantly upfield, *i.e.*, in a significantly more shielded environment, of that typically observed for protons in wide bandgap compounds,[37,38] has been assigned in the prior literature on BTO:H$^-$ to the presence of the hydride ion within the bulk of the material.[6,7,11] Thus, the relatively simple reaction of $NaBH_4$ with STO in an open environment indeed produces an oxyhydride.

Several additional peaks within the 0−10 ppm shift range, which vary erratically with reaction temperature, are also evident. These, which appear even in the case of the pristine STO (also included in Figure 2a), are assigned to surface species. In contrast to the bulk hydrogen, electronic shielding is not expected for resonances associated with surface species because there is no mixing of the atomic orbitals of the probed species and the electrons inducing metallic behavior in the bulk.[39] The presence of these additional resonances creates challenges in resolving the hydride peak when the extent of hydride incorporation is small or the concentration of surface species is large.

The bulk and surface assignments are supported by the spectra of the deuterated analog (reaction temperature of 400 °C). For reaction with $NaBD_4$, ^{2}H species are expected in the bulk, whereas ambient air exposure and H_2O used during washing would generate ^{1}H species on the surface. The ^{2}H spectrum of this material, Figure 2c, is dominated by a single peak at a shift of −9.8 ppm (assigned to bulk D-), whereas peaks at positive shift values (where the resonances of surface species are expected) are largely absent. The ^{1}H spectrum of this deuterated material (Figure S7) shows the reverse behavior: it is missing the bulk hydride peak, whereas peaks at 5 and 0 ppm are evident.

The spinning sideband manifold (shown in Figure S8) of the ^{2}H spectrum of STO:D- was analyzed to gain insight into the local structure. The analysis reveals the quadrupolar coupling constant, C_Q, to be 39 kHz and the asymmetry parameter, η, to be 0.01. The latter indicates that the macroscopic cubic symmetry is accompanied by a high local symmetry environment about the D- ion. The C_Q value is slightly larger than the value of ∼25 kHz reported for BTO:D- (D- content of 0.13−0.31 mol/F.U.).[6] Our EFG simulations, which show C_Q and Ti−D−Ti bond length to be inversely related (Figure S2), suggest that the discrepancy may be due to the longer Ti−D−Ti bond length in BTO:D-.

While the substitutional defect, $H_O^{\bullet}$ is the generally accepted form of the hydride ion in the literature on BTO:H-,[4−7,12,40] and the assignment is strongly supported by the results we report here as well as those in the prior literature,[5−7,11] the possibility of other sites of hydrogen incorporation cannot be immediately ruled out. As an example, if the perovskite hosts Schottky defects (charge balanced sets of cation and anion vacancies), with the Sr−O vacancy pair being particularly prominent in $SrTiO_3$,[41] hydrogen may be incorporated at those defect sites.[28] Shown in Table 1 are the NMR chemical shifts computed here for the most energetically favorable hydrogen containing defects,[28] where the defects are again described using Kröger-Vink notation. Because the impact of the Knight shift cannot be computed, the resonances of any of these defects could, in principle, align with the experimental observation of a peak in the 0 to −6 ppm range. However, in the case of the material prepared by reaction at 363 °C, the relatively small total reduction (quantified below) suggests a limited Knight shift and therefore a peak position that can be justifiably compared directly to the computed values. The experimental value of −1.46 ppm for this sample is in reasonable agreement with the computed value of −1.0 for the substitutional hydride defect, increasing confidence that $H_O^{\bullet}$ is the site of hydrogen incorporation.

The assumption that the sample reacted at 363 °C has a limited Knight shift raises the possibility that the downfield resonances in the 0 to 3 ppm range correspond to alternative compound defects involving cation site vacancies, with computed shifts ranging between 0.3 and 2.1 ppm. However, the absence of a correlation between reaction conditions and peak position, as well as the observation of resonances in this region for even pristine STO argues, as noted above, against such an assignment and instead indicates that these resonances reflect surface species. Because a Knight shift is not expected to impact surface species, the computed peak position for such species are, in principle, directly comparable to the experimentally measured positions. However, there are a plethora of possible arrangements of OH and H_2O groups on the surface of $SrTiO_3$,[30,42] and the relevant configuration is not immediately obvious. The calculation here for a single OH configuration already yields two resonances. Nevertheless, the computed shift values of 4.5 and 5.5 ppm for surface OH groups, being significantly downfield of the resonance of the bulk incorporated H species, correspond reasonably well to the sharp surface feature observed experimentally at 3.6 ppm.

Quantification of Anion Site Chemistry

Quantification of the chemical composition of the STO:H- materials requires that the products be free of impurity phases following the washing procedure. In previous work, Nedumkandathil et al. reported the emergence of a $BaTi(BO_3)_2$ phase following heat treatment to 900 °C of barium titanate

https://doi.org/10.1021/acs.chemmater.5c03181
Chem. Mater. 2026, 38, 4961−4974

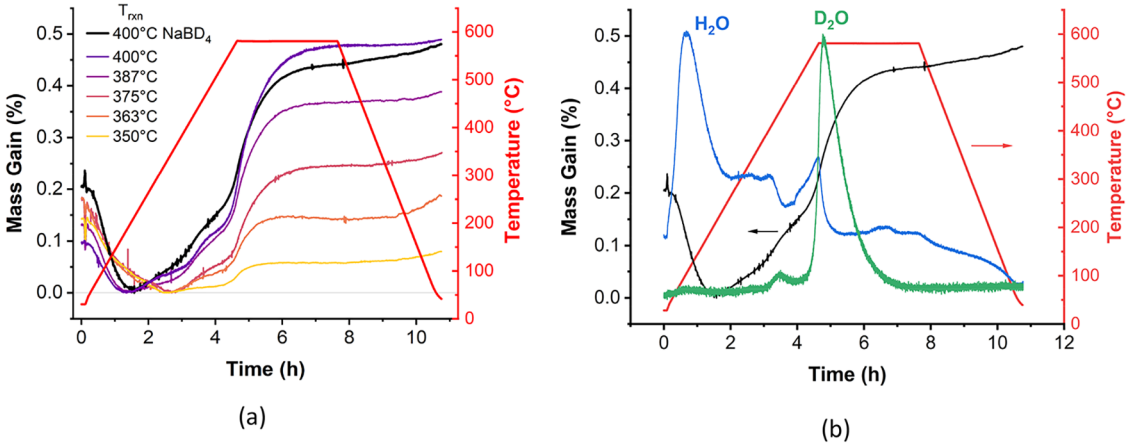

Figure 3. Thermogravimetric analysis of STO:D- and STO:H-: (a) Overlay of TGA profiles of samples obtained at the reaction temperatures indicated in the legend. The sample obtained from reaction with $NaBD_4$ (at 400 °C) is also included. Gas is a mixture of synthetic air (100 mL/min) and Ar (30 mL/min). (b) TGA-MS profile during reoxidation of the STO:D- fabricated at 400 °C. The ion current profiles corresponding to H_2O (blue) and D_2O (green) channels are plotted in arbitrary linear units. The isothermal hold (in both panels) is at 580 °C.

oxyhydride produced from reaction of $BaTiO_3$ and $NaBH_4$.[7] As shown in Figure S12, the diffraction patterns of all the materials after completion of an analogous high-temperature treatment revealed only the presence of the perovskite phase, arguing against the possibility that substantial amounts of amorphous phases were retained following the synthesis. Several reasons could account for the differences including the differing reaction configurations (flowing gas to remove evolved species *vs* a sealed environment), the use of different solvents to wash the products, and inherent differences in behavior between $SrTiO_3$ and $BaTiO_3$. The ^{11}B NMR spectrum collected from the T_{rxn} = 400 °C sample (Figure S11) similarly indicated negligible B containing compounds in the washed product mixture of this work. Specifically, the spectrum indicated that residual boron impurities are present in only very low concentrations, estimated to be 6×10^{-4} wt %.

The hydride content was directly determined from the quantitative NMR analysis (in which adamantane was used as an internal standard). The peak deconvolution is presented in Figure S10. The hydride concentration is obtained from the relative integrations of the hydride and adamantane peaks and the relative masses of the two components (eq S1). In the case of the sample prepared at 350 °C, it was not possible to confidently identify a hydride peak, whereas in the case of the sample prepared at 425 °C, despite a prominent hydride peak, the high signal from surface species, presumably resulting from the ethanol wash, prevented confident evaluation of the peak integrals (Figure S6a). The results for the samples that could be successfully analyzed are provided below, alongside the chemical analysis derived from the TGA measurements.

The TGA profiles of the STO:H- and STO:D- materials were in all cases characterized by an initial mass loss, followed by a multistep mass gain, Figure 3a. The data furthermore reveal a monotonic increase in mass gain with reaction temperature from 350 to 400 °C, Figure 3a, consistent with the overall features of the NMR spectra, Figure 2. To enable the interpretation of these profiles, the exhaust gas from a TGA experiment for the deuterated (T_{rxn} = 400 °C) sample, Figure 3b, was analyzed. The combined TGA-MS data show clear mass loss and elevated H_2O signal up to 180 °C, with no detectable release of D_2O (or CO_2). This low-temperature mass loss is thus interpreted to reflect the removal of surface sorbed water (and hydroxyl) species. The other alternative, release of bulk oxygen, requires much higher temperatures and/or much lower oxygen chemical potentials than the air environment of the experiment. The absence of D_2O from the evolved gases in this temperature range indicates that the surface species were adsorbed on the material after synthesis, when the material was no longer in contact with a deuterium source. This conclusion is supported by the ^2H NMR spectrum discussed above, Figure 2c, which is largely free of resonances from ^2H surface species.

The TGA mass gains, Figure 3, complete in two minor steps followed by one major step. Taking the deuterated material as an example (Figure 3b), the mass increases slightly from 180 to 400 °C, then there is a somewhat more abrupt, but still minor, gain at 400 °C which is accompanied by a gradual tail extending to about 540 °C. In the final step, the mass increases sharply over the temperature range from 550 to 580 °C, with mass gain continuing well into the isothermal hold. Throughout the first step of mass gain, the H_2O signal in the MS remains elevated relative to its final value, indicating that some of the change in mass in this regime (though dominated by mass gain) is due to continued loss of surface species. The second step is accompanied by a decrease in the H_2O MS signal and a very minor peak in the D_2O signal at 435 °C. The partial temporal overlap between loss of surface species and reoxidation may be responsible for the splitting of the lower-temperature mass gain into two distinct steps. The slight underestimation of the total reduction due to this simultaneous reoxidation and removal of surface species in the initial steps is no more than 0.01 mol/F.U. based on the integration of the MS signal. In the final step, the dominant mass gain event is accompanied by a large spike in release of D_2O at 580 °C. The peak in the H_2O signal that appears at approximately the same time is likely due to spillover in the MS channels. Overall, these features suggest that the first two mass gains are largely due to the filling of oxygen vacancies and that the final is due to deuterium/oxygen exchange accompanied by deuterium oxidation.

Based on the interpretation of the mass profile for the deuterium-containing material, the total reduction for all materials was derived from the difference between the

https://doi.org/10.1021/acs.chemmater.5c03181
Chem. Mater. 2026, 38, 4961−4974

minimum and maximum mass values, Figure 3a (taking the impact of hydrogen content on the mass to be negligible). This total reduction amount was then divided into the portion given by the two lower temperature mass gain steps and that given by the higher temperature mass gain event. Full details of the analysis are provided in the SI (eqs S4–S6 and Table S5). The total TGA-determined reduction, with the portions loosely assigned to hydride content (from the mass gain at high temperature) and anion vacancies (from the two-step mass gain at low temperature) distinguished, is compared in Figure 4 to the hydride content determined by quantitative NMR

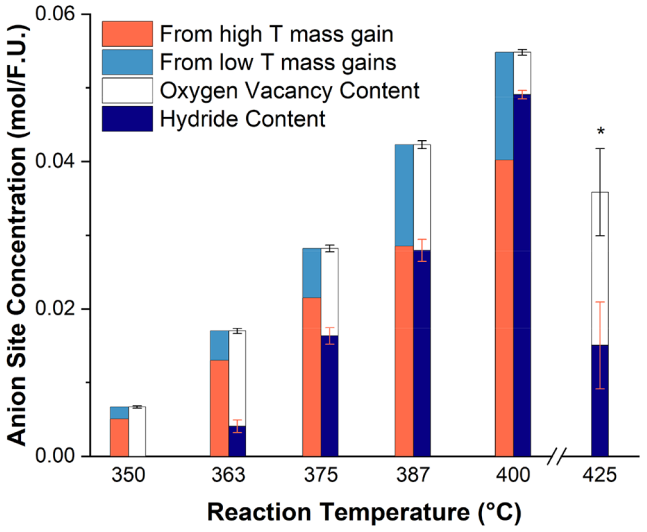

Figure 4. Comparison of the anion site chemistry in STO:H- determined by TGA and by NMR spectroscopy as a function of reaction temperature. The mass gains in TGA are converted to anion site concentrations. The oxygen vacancy content is taken to be the difference between the total TGA-derived anion deficiency and the NMR-derived hydride content. *Due to significant amounts of surface species, values are estimated from the ^{1}H shift position and EPR signal, as described in the SI.

spectroscopy. There is reasonable correlation between the two regions of mass gain and the anion defect types. Figure 4 includes data for the hydride and vacancy concentrations of the material prepared by reaction at 425 °C. The manner by which these values was estimated is described below.

The derived chemical formulas, denoting the full anion chemistry, are summarized in Table 2. The vacancy concentration reported is that obtained from the difference between the total TGA-determined reduction and the hydride

Table 2. Sample Compositions Determined through TGA and Quantitative NMR; Formulas Written as $SrTiO_{3-x}H_y$

T_{rxn} (°C)	^{1}H shift (ppm)	anion vacancy concentration (mol/f.u.)	final formula
425	−3.84	0.021 ± 0.006	$SrTiO_{2.964}H_{0.015}$[a]
400	−5.22	0.0057 ± 0.0004	$SrTiO_{2.945}H_{0.049}$
387	−4.22	0.0143 ± 0.0006	$SrTiO_{2.958}H_{0.028}$
375	−3.57	0.0119 ± 0.0005	$SrTiO_{2.972}H_{0.016}$
363	−1.92	0.0129 ± 0.0004	$SrTiO_{2.983}H_{0.004}$
350	N/A	0.0067 ± 0.0002	SrTiO2.993

[a]Composition of the 425 °C sample is estimated from the ^{1}H shift and EPR as described in the SI.

content, yielding a result that is independent of the details of the mass uptake profiles. Surprisingly, the vacancy concentration varies somewhat erratically with reaction temperature. At T_{rxn} = 400 °C, the oxyhydride incorporates only approximately 1.1% of the hydrogen available from the $NaBH_4$. Nevertheless, at reaction temperatures of 375 to 400 °C, the hydride content exceeds the vacancy content, indicating that hydride incorporation is favored over simple removal of oxygen at these conditions.

Electronic and Defect Structure

In BTO:H-, the strong upfield shift of the hydride NMR resonance has been attributed to the electrically conducting nature of the material.[6] Metallicity is induced by excess electrons that balance the $H_O^{\bullet}$ and $V_O^{\bullet\bullet}$, leading to the Knight shift introduced above.[6,35] For simple metals, in which the conduction bands have significant s-orbital character, the applied magnetic field induces a spin polarization of the conduction electrons, producing a Fermi-contact hyperfine field that adds to the magnetic field experienced by the nucleus. The Knight shift thus manifests as a downfield shift.[43] In the case of transition metals with partially filled d-orbitals at the Fermi level, such as Ti^{3+}, the exchange interaction of unpaired d-electrons with those in the filled s-orbitals of the hydride results in an excess of opposite-spin electrons in the hydride s-orbitals. This excess opposite-spin density at the nucleus generates a negative Fermi-contact shift for the hydride species, as observed here. An alternative model has been proposed by Misaki et al.,[44] in which the nuclear shielding is attributed to occupancy on the hydride sites by two hydrogen atoms. There is no evidence of such a configuration in the present study.

In a material in which the ^{1}H NMR shift is dominated by such Fermi contact interactions, conduction electrons at the Fermi level provide a fluctuating magnetic field at the nucleus, which facilitates the energy transfer required for spin relaxation. Accordingly, the spin–lattice relaxation time, T_1, as measured as a function of temperature, is inversely correlated to the square of the shift.[45] This is recognized as the Korringa relationship, and such behavior has been observed for oxyhydride materials.[6] Here, across multiple STO:H- samples with different $H_O^{\bullet}$ concentrations and measured at a fixed temperature, we observe a "Korringa-like" pattern, where $1/T_1$ is approximately linear with ^{1}H shift (Figure S9). Our data are consistent with the hyperfine interactions between the ^{1}H spins and conduction electrons at the Fermi level acting as the major mechanism driving the ^{1}H spin–lattice relaxation.

The EPR measurements reveal the nature of the electronic defects in STO:H- (at 10K), Figure 5. The spectra, Figure 5a, display a sharp feature at a g-value of 2.00, characteristic of free electrons,[46,47] along with other features which vary with reaction temperature. For the less-reduced samples (T_{rxn} = 350, 363 °C), a second sharp feature is observed at a g-value of 1.97, characteristic of unpaired electrons localized on a Ti atom, making the cation effectively Ti^{3+}.[48,49] As the reaction temperature is increased (T_{rxn} = 375–400 °C), this signal is obscured by a broad feature at a g-value of 1.93. In light of the large hydride content of these materials, this feature is assigned to Ti^{3+} neighboring H^-. The spectrum of the T_{rxn} = 425 °C material is rather distinct from the others. Here, a strong resonance at g = 1.99 emerges and can be attributed to oxygen

https://doi.org/10.1021/acs.chemmater.5c03181
Chem. Mater. 2026, 38, 4961–4974

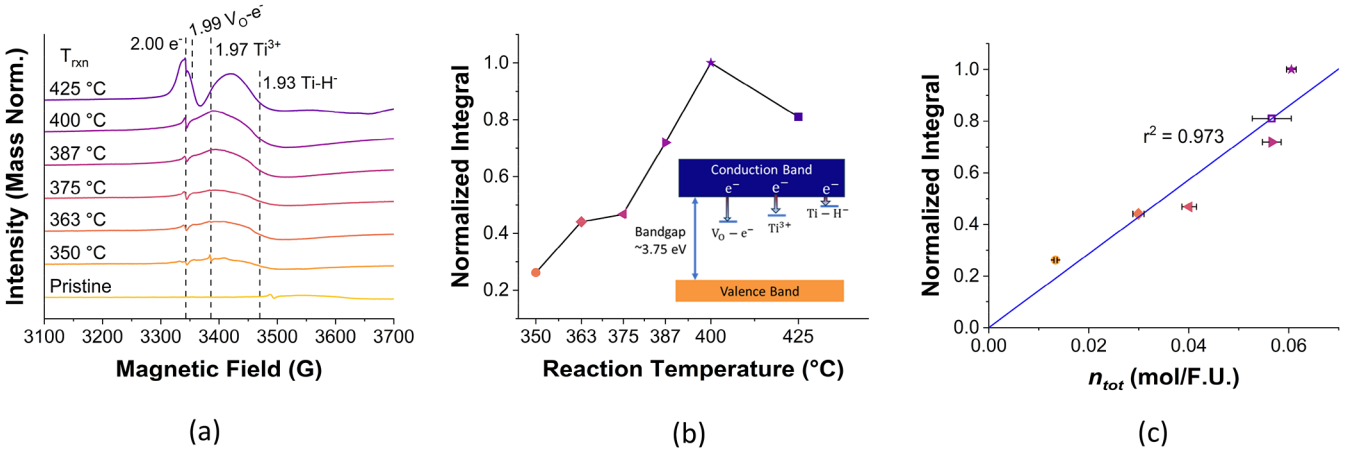

Figure 5. Results of EPR measurements: (a) spectra with *g*-values of each feature indicated by dashed lines, (b) normalized integral of the total absorptive EPR signal between 3000 and 4000 G as a function of reaction temperature (full spectra are shown in Figure S15), and (c) integral EPR signal against the carrier concentration determined through TGA and NMR (see text). The inset in (b) schematically shows possible positions of the defect states relative to the band edges. The open square in (c) for 425 °C is computed from the observed trend.

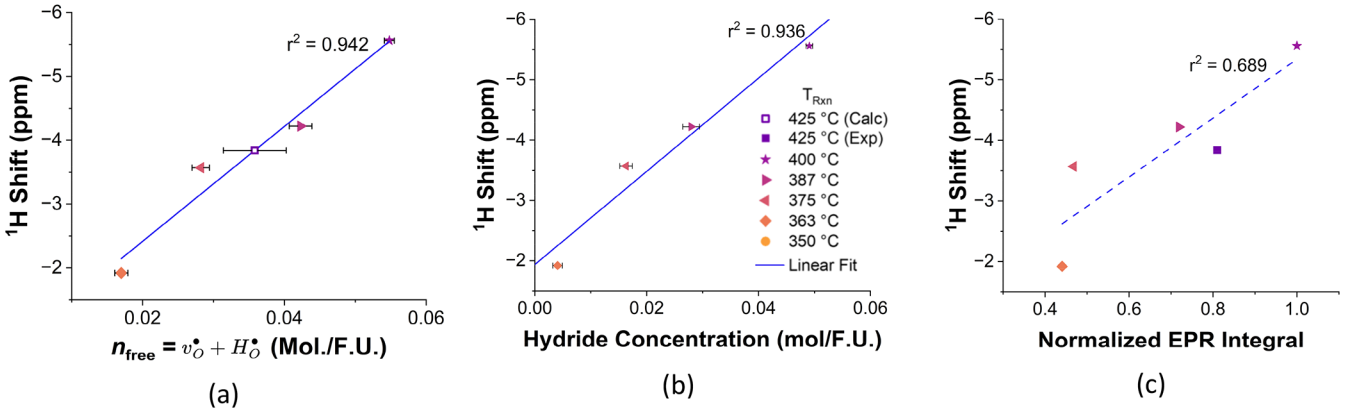

Figure 6. Trends observed between ^{1}H shift and defect chemistry, where latter is defined as (a) free carriers, given by sum of oxygen vacancy concentration and hydride concentration; (b) hydride concentration; and (c) unpaired electrons, given by EPR signal integral.

vacancies.[49,50] The schematic inset in Figure 5b is intended to guide the interpretation of spectral features.

The total concentration of electronic defects (n) in STO:H- is formally given by $n_{tot} = 2[v_O^{\bullet\bullet}] + [H_O^{\bullet}]$. Presuming these electrons are unpaired, the total integrated EPR signal intensity, Figure 5b, is expected to be directly proportional to this concentration. From the NMR and TGA measurements, we obtain the values of $[v_O^{\bullet\bullet}]$ and $[H_O^{\bullet}]$ and thus an independent determination of n_{tot}. As shown in Figure 5c, the expected correlation between EPR signal intensity and electronic defect concentration is observed.

Beyond revealing the nature of the electronic defects and their total concentration, the EPR measurement, along with the independent measurement of the hydride concentration, allows an exploration of the electronic origin of the Knight shift. As the spin polarization of the hydride 1s-orbital is induced by the electrons in the conduction band (*i.e.*, near the Fermi level, mostly Ti-3d), the magnitude of the Knight shift is expected to be related to the concentration of band-state electrons. This concentration may be distinct from the n_{tot} reflected in the total EPR signal if a portion of the electrons are trapped. In the case of oxygen-deficient $SrTiO_{3-\delta}$, which has been the subject of numerous studies due to the reports of simultaneous *n*-type conductivity and blue luminescence,[51,52] there is general agreement that the vacancy serves as a double donor, from which one electron is easily excited, while the other electron is deeply trapped.[52] If this behavior also occurs in STO:H-, then each anion vacancy is charge balanced by only one electron in the conduction band. In such a scenario, the concentration of electronic defects that are expected to contribute to the Knight shift is given by $n_{free} = [v_O^{\bullet}] + [H_O^{\bullet}]$. Alternatively, the anion vacancies could each trap two electrons, such that n_{free} is simply equal to the hydride concentration, or the vacancies could be fully unoccupied (with no trapped electrons), such that $n_{free} = n_{tot}$. Shown in Figure 6 are the correlations of the ^{1}H shift with these three possible scenarios. We observe the strongest agreement between shift and electron concentration for the model in which oxygen vacancies trap one electron, Figure 6a. Significantly, the *y*-intercept in Figure 6a is an extrapolation to the shift for a sample with no free electronic carriers. The value, −0.62 ppm, is in close agreement with the computed value for $H_O^{\bullet}$ of −1.0 ppm.

Figure 6c shows that there is poor correlation between the EPR signal and the ^{1}H shift, supporting the conclusion that oxygen vacancies, the concentrations of which vary erratically with synthesis temperature (Table 1), trap electrons at the ambient temperature of the NMR measurements. On the other hand, the correlation between hydride concentration and ^{1}H shift is significant, Figure 6b. At first glance, this contradicts the

https://doi.org/10.1021/acs.chemmater.5c03181
Chem. Mater. 2026, 38, 4961−4974

interpretation that the concentration of electrons that induce the shift is given by $[v_O^{\bullet}] + [H_O^{\bullet}]$. However, for three of the four data points shown in Figure 6b, the vacancy concentration is effectively constant (363, 375, 387 °C), and in the fourth case (400 °C), the vacancy concentration is substantially lower than the large hydride concentration (Table 1). These effects conspire to generate an approximately linear correlation with $[H_O^{\bullet}]$. In selected prior studies, the ^{1}H shift was shown to be linearly correlated to the hydride concentration.[7,44] A plausible explanation for those observations is that the synthesis conditions of those studies results in a correlation between the anion site vacancy concentration and the hydride concentration.

The correlations presented in Figures 5c and 6a enable, respectively, estimation of the concentration of electronic defects, n_{tot} and n_{free}, in the sample prepared using T_{rxn} = 425 °C. The results are included in the figures. With n_{tot} and n_{free} both known, $[v_O^{\bullet}]$ and $[H_O^{\bullet}]$ are easily obtained as described in the SI, eqs S2−S3. Through this analysis, we observe the hydride content in the T_{rxn} = 425 °C material to be lower than that of the T_{rxn} = 400 °C material, whereas the vacancy content is higher (Figure 4). This agrees with the large EPR resonance at g = 1.99, assigned to oxygen vacancies that is observed in the T_{rxn} = 425 °C material.

Reaction Pathway and Influences on Hydride Uptake

Several aspects of the preparation of STO:H- from reaction of STO with $NaBH_4$ are noteworthy. Most significant is the nonmonotonic dependence of hydride content on T_{rxn}. The formation of STO:H- by the direct pathway, eq 1, can be expected to be thermodynamically favored with increasing temperature because the reaction evolves gaseous H_2O as a byproduct. Thus, one might anticipate that the hydride content in the oxyhydride would increase monotonically with T_{rxn}, in contradiction to what was observed. The known decomposition of $NaBH_4$ ($\Delta H^0 = -108$, $\Delta S^0 T = 89.5$ at 400 °C, $\Delta G^0 = -197.5$, all in kJ/mol[18])

$$\frac{1}{2}NaBH_4(s) \rightarrow \frac{1}{2}\sum_i \text{solid(Na, B)}_i + H_2(g) \quad (2)$$

raises the possibility of a different pathway to oxyhydride formation in which the reaction occurs by a sequential process involving decomposition to release H_2 which then reacts with the oxide. Because reaction 2 is also favored with increasing temperature, this scenario should also result in an increase in hydride content with T_{rxn}. Thus, one might expect that for either pathway, the hydride content in the oxyhydride would increase monotonically with T_{rxn}. The decline in hydride content beyond T_{rxn} = 400 °C suggests a mechanism that interferes with hydride uptake at high temperature. We propose that the oxyhydride forms by the direct pathway and the decomposition of $NaBH_4$ at $T \geq 425$ °C interferes with the product formation by decreasing the concentration of this vital solid-state reagent.

There has been some attempt in the literature to determine the relative roles of solid−solid and gas−solid reactions using hydride precursors, from which it was concluded that no single answer applies to all syntheses.[16,53] On the other hand, the direct pathway is supported by literature indicating that perovskite titanate oxyhydrides cannot be formed by simple reaction of H_2 with oxides at ambient pressure.[7] In the analogous case of oxynitride synthesis, it is known that NH_3 reacts far more readily with oxides than N_2 does. The oxynitride synthesis is understood in terms of the higher chemical potential of the reactant species (nitrogen) when it is in the form of ammonia than when it is in the form of dinitrogen,[54] and the same may hold here for hydrogen when it is present in sodium borohydride *versus* when it is in the form of dihydrogen.

If the formation of STO:H- were to occur by reaction with gaseous H_2, then the diminishing hydride content beyond the optimal reaction temperature of ∼400 °C could possibly be explained by too rapid a removal of the H_2 generated from the thermally enhanced decomposition. That is, the Ar gas flow, introduced to remove the expected product H_2O (eq 1), removes the generated H_2 (even though the equilibrium concentration is low at these temperatures[18]) before it has sufficient time to react with the oxide. If true, then supplying H_2 rather than Ar would be expected to enhance the extent of hydride incorporation. In fact, the opposite was observed. When the gas was changed from Ar to H_2, the lattice parameter matched that of pristine STO (Figure S3b) and no hydride peak was detected in the NMR spectrum (Figure S6b), though the spectrum was notably distinct from that of pristine STO. The material underwent a mild change in color to a pale blue, suggesting slight reduction. Because the thermodynamics of hydride formation should be favorable under H_2, we propose that the near-absence of hydride uptake may be due to sluggish surface reaction kinetics in the presence of hydrogen. The distinctive surface feature in the ^{1}H NMR spectrum of the material resulting from the reaction under H_2 provides some support for this hypothesis (Figure S6b). Thus, gaseous H_2 generated from decomposition of $NaBH_4$, as in eq 2, is not the source of the incorporated hydride ions, leaving the direct reaction as the only possible pathway. Accordingly, oxyhydride formation is bypassed when the reaction temperature is so high that the precursor undergoes decomposition, where decomposition here refers explicitly to release of gaseous H_2.

Before turning to the *in situ* studies aimed at directly revealing the reaction pathway, it is valuable to first consider the nature of the full set of products (*i.e.*, not washed) generated from a reaction temperature at 425 °C. The XRD pattern of this material reveals peaks which appear to match those of metallic Na, Figure 7, Figure S5. The remaining peaks are fully attributable to the oxyhydride and a small amount of residual $NaBH_4$. Notably, reaction of Na with liquid water to form NaOH and H_2 is highly favorable at ambient temperature and would occur with a standard enthalpy of −140 kJ/mol (Na). The reaction with aqueous CO_2 is even more favorable and even more exothermic.[55] Thus, in principle, the presence of Na in the reaction product could explain the sparking observed when contacted with water and the increased reactivity when the water contained dissolved CO_2. However, metallic Na melts at 98 °C, and the material removed from the reaction vessel showed no physical evidence that a component in the mixture had been molten at any point in the reaction.

The lack of evidence of molten phases during the reaction raises the possibility that the peaks which seemingly match Na are due to a different phase. A search through plausible candidates yielded NaH, a computationally predicted compound with the B2 or CsCl structure type, as a phase that matched the peaks (OQMD entries 305282 and 23862[56,57]). Refinement against the measured XRD data, Figure 7, shows an excellent fit with a final R_{wp} of 6.83%. The refined phase mixture is composed of 93.9 wt % cubic STO (a_0 = 3.90508(4) Å), 3.9 wt % cubic NaH (a_0 = 3.0311(3) Å), and balance

https://doi.org/10.1021/acs.chemmater.5c03181
Chem. Mater. 2026, 38, 4961−4974

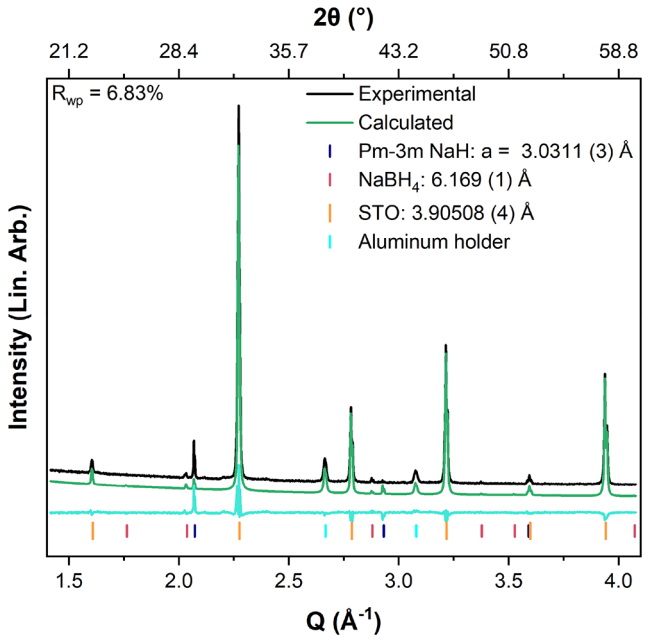

Figure 7. XRD pattern of the unwashed reaction products from a reaction at 425 °C, collected using an airtight sample holder. Upper scale reports 2θ for Cu Kα radiation.

$NaBH_4$. The cell parameter of NaH is almost precisely $\sqrt{2}\times$ that of BCC Na (4.2872 Å), making the two patterns indistinguishable in X-ray diffraction without extending to large Q. Thus, refinement with Na, Figure S5, yielded a similar fit to refinement with NaH.

The *in situ* thermal analysis, Figure 8, reveals several features of the reaction pathway. In the DSC trace, an exothermic event initiates at ~340 °C, which coincides with the initiation of substantial detection of D_2 and D_2O in the mass spectrometer

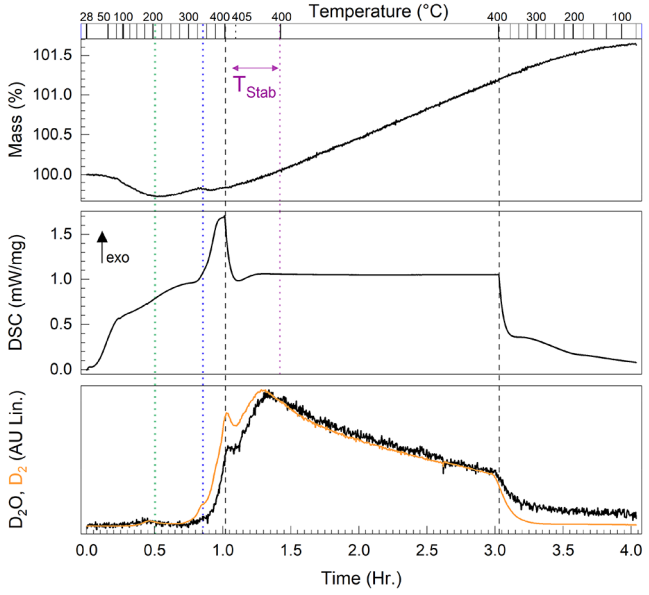

Figure 8. *In situ* monitoring of the reaction between STO and $NaBH_4/NaBD_4$ as recorded by STA ($NaBH_4$, upper two panels), and by in-line MS detection of the exhaust gases from the standard tube furnace configuration ($NaBD_4$, lower panel). The experiments were conducting independently with identical programming; temperatures are those recorded by the STA instrument.

and is consistent with the exothermic nature of the decomposition of $NaBH_4$ (eq 2). The release of D_2O along with the D_2 suggests that the $NaBD_4$ decomposition is accompanied by reaction with the oxide. Both measurements (which were performed independently) reveal the effects of thermal overshoot when the programmed dwell time (at 400 °C) begins. The exothermic response immediately declines as the temperature decreases following the brief overshoot, then stabilizes to a finite value during the hold. The D_2 and D_2O signals similarly peak at 400 °C, but then each display a second broad peak that occurs approximately 15 min into the hold period. The overall behavior indicates that decomposition of $NaBH_4$ rises rapidly between 350 and 400 °C, then gradually declines over time. The thermal analysis further reveals notable mass gain. This is attributed to oxygen leaks into the system. The total mass gain equates to approximately 0.21 mol O per mole $NaBH_4$, and thus a small amount of oxidized products of $NaBH_4$ (such as sodium hydroxide or boron trioxide) could account for the observation. The mass profile is clearly distinct from the DSC profile, implying that oxidation cannot account for the large DSC peak, which corresponds much more closely to $NaBD_4$ decomposition reflected in the MS signals.

The *in situ* XRD studies of the reaction carried out at T_{rxn} = 400 °C, Figure 9, and 425 °C, Figure S4c, show that the

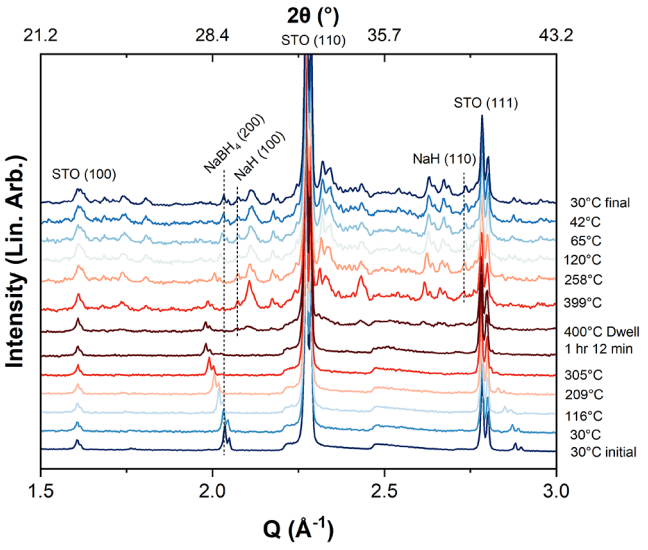

Figure 9. *In situ* XRD patterns of a 1:1 molar mixture of $NaBH_4$ and STO upon heating to and holding at 400 °C, with identified peaks indicated with dashed lines. $NaBH_4$ undergoes significant thermal expansion and the peaks corresponding to this phase visibly shift to smaller Q on heating, whereas the STO peaks remain relatively fixed. The feature at ~2.4 $Å^{-1}$ is the Sr K-edge. Upper scale reports equivalent 2θ for Cu Kα radiation.

patterns are largely unchanged from the initial room temperature measurement to the first measurement at T_{rxn}, other than steady thermal expansion of $NaBH_4$. In both cases, multiple peaks of poorly crystalline phases appear during the hold period and are retained in the final room temperature product. This significant difference from the *ex situ* measurement is attributed to the difference in gas flow configuration between the two experiments. In the horizontal flow reactor moderately volatile products are steadily removed whereas they are deposited onto the fine mesh sample holder in the XRD. The plethora of possible Na−B−O−H solids hindered

https://doi.org/10.1021/acs.chemmater.5c03181
Chem. Mater. 2026, 38, 4961−4974

identification of the product phases. Significantly, in both *in situ* XRD experiments, the peaks attributed to NaH begin to form at T_{rxn}, confirming that the peaks cannot be due to metallic sodium which melts at 98 °C. In contrast to Na, the experimentally reported phase of NaH is known to be stable to 800 °C.[58] At the conclusion of the experiment, exposure of the sample to air was observed to degrade the Na-bearing phase (Figure S4d), as would be expected for either NaH or Na.

An important difference between the two reaction conditions is that while the $NaBH_4$ experiences partial decomposition at T_{rxn} = 400 °C, the peaks from the borohydride are almost entirely absent in the pattern obtained after an hour at T_{rxn} = 425 °C. Complete decomposition of $NaBH_4$ at 425 °C is consistent with the proposal that hydride incorporation into the perovskite occurs primarily *via* solid−solid reaction. At this high temperature, simple decomposition of the reagent proceeds, bypassing the targeted reaction.

Like sodium, sodium hydride is known to react violently with water and with water containing dissolved CO_2. Both reactions (given below) release H_2, which is highly combustible

$$NaH(s) + H_2O(l) \rightarrow NaOH(aq) + H_2 \quad (3)$$

$$2NaH(s) + CO_2(aq) + H_2O(l) \rightarrow Na_2CO_3(s) + 2H_2 \quad (4)$$

Similar to metallic sodium, these reactions are quite exothermic. The standard enthalpy of reaction (3) is −84 kJ/mol(Na).[55,59] In the case of the formation of the carbonate from a solution in equilibrium with 1000 ppm of CO_2 in the atmosphere the enthalpy of reaction (4) is extremely large in magnitude, −170 kJ/mol. In the present experiments, degassing eliminated sparking for materials produced at $T_{rxn} \leq 400$ °C, but not completely for the material produced at T_{rxn} = 425 °C. This is consistent with the greater level (and potentially complete) decomposition of $NaBH_4$ at T_{rxn} = 425 °C, which then results in a higher proportion of NaH in the product.

The presence of NaH as a product of the reaction between STO and $NaBH_4$ indicates that the global reaction chemistry differs from the targeted reaction of eq 1. While not every product has been identified, a simplified reaction that generates only NaH as the Na-bearing product is expressed as

$$SrTiO_3(s) + xNaBH_4(s) \rightarrow SrTiO_{3-3x}(s) + xNaH(s) + \frac{x}{2}B_2O_3(s) + \frac{3x}{2}H_2O(g) \quad (5)$$

This reaction inherently results in a negligible hydride content in the perovskite in contrast to the idealized reaction pathway in which $NaBO_2$ is the byproduct, eq 1. When sodium hydride is the product, the sodium, rather than contributing to reducing the oxide, competes to retain hydrogen. This can be understood as a consequence of the relatively small (in magnitude) ΔG for NaH oxidation and is consistent with prior work which demonstrated NaH fails to hydride BTO.[7] The greater effectiveness of CaH_2 in generating oxyhydrides than $NaBH_4$ and NaH may then reflect the larger (in magnitude) ΔG for Ca oxidation than Na oxidation. The complete reaction pathways are undoubtedly more complex than eqs 1 and 5, but it is apparent that, overall, the solid−solid reaction pathway is possible at moderate temperatures, peaking at ∼400 °C, and at higher temperatures, the decomposition of $NaBH_4$ is increasingly favored.

A final aspect of the reaction warrants brief attention. Somewhat surprisingly, neither increasing the reaction time (from 1 to 2 h), nor decreasing the $NaBH_4$:STO molar ratio (from 1:1 to 0.5:1) had a noticeable impact on the perovskite, as characterized by ^{1}H NMR (Figure S6a) and XRD (Figure S3b). The in-line MS data collected during the reaction between STO and $NaBD_4$ (Figure 8) reveals that the rate of $NaBD_4$ reaction with the STO, as reflected in the D_2O signal, decreases after the first hour of the isothermal hold at 400 °C. This is consistent with the observation that an increase in reaction time has little effect on the hydride content. Moreover, the low total concentration of D_2O, as indicated by the poor S/N in this channel, demonstrates that even at the peak of the reaction, the amount of water released is small relative to the deuterium (hydrogen) released. This result is consistent with the low extent of hydride incorporation in the final product, though it does not directly address the evidently strict decline in incorporation after 1 h. The reason for the insensitivity of the extent of hydride incorporation to a decrease in $NaBH_4$ reactant relative to STO is also not entirely obvious. These observations point to a subtle interplay between the driving forces for the solid−solid reaction and the gas phase decomposition of $NaBH_4$.

CONCLUSIONS

In this work, we demonstrate that STO:H- can be formed through a simple reaction between $SrTiO_3$ and $NaBH_4$ in an open system and occurs in a shorter time and at significantly lower temperatures than conventionally used for reaction with CaH_2. The synthesis yields a similar amount of hydride substitution as has been reported for reaction with $NaBH_4$ under vacuum at 600 °C for 2 days using a 0.3:1 molar ratio of $NaBH_4$:BTO,[7] while being easier and safer to implement. In addition, the final composition is readily controlled through variation of reaction temperature. Increasing temperature initially favors hydride incorporation, but when the temperature is too high (>400 °C), decomposition of the $NaBH_4$ and loss of H_2 to the gas phase become favored over reaction with the oxide. The thermal trend reflects the incorporation of hydride into the perovskite from $NaBH_4$ *via* a direct solid−solid reaction rather than by reaction of the oxide with H_2 generated from the decomposition of the hydride precursor. Significantly, NaH with the B2 crystal structure, a computationally predicted but not previously experimentally realized compound, was identified as a high-temperature reaction product stable at 425 °C. Retention of hydrogen in this compound is unfavorable for hydride incorporation into the perovskite lattice. Separately, the surprising observation that introduction of H_2 into the Ar flow, where Ar is supplied to remove the product gases, entirely prevents hydride incorporation suggests surface poisoning that impedes the desired reaction.

^{1}H NMR studies of these materials fully support the assignment of the shielded peak, occurring in the shift range from −1 to −6 ppm, to a hydride species, with surface species responsible for peaks in the 0 to 10 ppm range. The atypical direction of the Knight shift results from the exchange interaction of unpaired d-electrons in the conduction band with those in the filled s-orbitals of the hydride. Direct measurements of the Ti-local environment using EPR

https://doi.org/10.1021/acs.chemmater.5c03181
Chem. Mater. 2026, 38, 4961−4974

measurements show that as the reaction temperature increases to 400 °C, the overall concentration of unpaired electrons increases. The features in the spectra could be assigned to (i) free electrons, (ii) localized electrons at Ti (effectively Ti^{3+}), (iii) localized electrons at Ti that neighbor hydride species, and (iv) localized electrons at anion vacancies. The feature due to anion vacancies is particularly prominent for the material obtained at T_{rxn} = 425 °C. The picture of the room temperature electronic structure that emerges of these materials is one in which anion vacancies trap single electrons and the concentration of conduction band electrons equals the sum of the vacancy concentration and the hydride concentration ($n_{free} = [v_O^{\bullet}] + [H_O^{\bullet}]$). By combining quantitative NMR, TGA, and EPR measurements, it was possible to fully define the anion site stoichiometry. At reaction temperatures of 375 °C−400 °C, the hydride content exceeds the vacancy content, and thus reactions of oxides with $NaBH_4$ should not overlook the possibility of hydride incorporation.

Overall, the simplicity of this reaction scheme, in combination with the short reaction times required and evidence of its viability for a broad range of materials, opens pathways for the widespread exploration of the properties and applications of oxyhydrides. Furthermore, more precise control of the gas phase chemistry than employed here, including elimination of trace O_2 and H_2O, may enable higher hydride incorporation.

■ ASSOCIATED CONTENT

Data Availability Statement

All study data are included in the article and/or Supporting Information. Raw data from this study, as well as the DFT structures, are available at: https://osf.io/x5skr/overview?view_only=ea5bdee97160461292b552d84619f2ca.

Supporting Information

The Supporting Information is available free of charge at https://pubs.acs.org/doi/10.1021/acs.chemmater.5c03181.

DFT reference compounds, DFT EFG simulations, XRD overlay and lattice expansion, NMR of additional synthesis conditions, details and fitting of the quantitative NMR spectra, residual impurity analysis, SEM, and TGA data (PDF)

■ AUTHOR INFORMATION

Corresponding Author

Sossina M. Haile − *Department of Materials Science and Engineering, Northwestern University, Evanston, Illinois 60208, United States;* orcid.org/0000-0002-5293-6252; Email: sossina.haile@northwestern.edu

Authors

Megan E. Burrill − *Department of Materials Science and Engineering, Northwestern University, Evanston, Illinois 60208, United States;* orcid.org/0000-0002-1218-085X

Islamiyat Ojelade − *Department of Chemistry and Biochemistry, Florida State University, Tallahassee, Florida 32306, United States*

Erica Truong − *Department of Chemistry and Biochemistry, Florida State University, Tallahassee, Florida 32306, United States*

Tomas Orlando − *National High Magnetic Field Laboratory, Tallahassee, Florida 32310, United States;* orcid.org/0000-0001-7261-2119

Rongfu Zhang − *Department of Chemistry and Biochemistry, Florida State University, Tallahassee, Florida 32306, United States*

Yan-Yan Hu − *Department of Chemistry and Biochemistry, Florida State University, Tallahassee, Florida 32306, United States; National High Magnetic Field Laboratory, Tallahassee, Florida 32310, United States;* orcid.org/0000-0003-0677-5897

James M. Rondinelli − *Department of Materials Science and Engineering, Northwestern University, Evanston, Illinois 60208, United States;* orcid.org/0000-0003-0508-2175

Complete contact information is available at: https://pubs.acs.org/10.1021/acs.chemmater.5c03181

Author Contributions

M.E.B. performed sample synthesis. M.E.B, I.O., and E.T. carried out the experiments with support from T.O. and R.Z. and supervision from S.M.H. and Y.Y.H. M.E.B. performed the simulations with supervision from J.M.R. M.E.B wrote the manuscript with input from all authors. All authors provided feedback to help shape the research, analysis, and manuscript. S.M.H, J.M.R., and Y.Y.H secured the resources.

Notes

The authors declare no competing financial interest.

■ ACKNOWLEDGMENTS

The authors would like to thank the Northwestern shared facilities staff for their assistance and advice, namely Jinlei Cui at the Integrated Molecular Structure Education and Research Center (IMSERC) and Sumit Kewalramani at Jerome B. Cohen X-ray Diffraction Core Facility. Additionally, we are extremely thankful to Davide Ceresoli for his suggestions regarding the NMR simulations and additional pseudopotentials. We would also like to thank Clare Grey for her discussions about NMR simulations. This research was primarily supported by the Hydrogen in Energy and Information Sciences (HEISs) EFRC, an Energy Frontier Research Center funded by the U.S. Department of Energy (DOE), Office of Science, Basic Energy Sciences (BES), under Award #DE-SC0023450. This work made use of the IMSERC (RRID:SCR 017874) NMR facility at Northwestern University, which has received support from the Soft and Hybrid Nanotechnology Experimental (SHyNE) Resource (NSF ECCS-2025633), International Institute of Nanotechnology, and Northwestern University. This work made use of the Northwestern University Jerome B. Cohen X-ray Diffraction Core Facility (RRID:SCR_017866) supported by the MRSEC program of the National Science Foundation (DMR-2308691) at the Materials Research Center of Northwestern University. This research was supported in part through the computational resources and staff contributions provided by the Quest high performance computing facility at Northwestern University which is jointly supported by the Office of the Provost, the Office for Research, and Northwestern University Information Technology. A portion of this work was performed at the National High Magnetic Field Laboratory, which is supported by National Science Foundation Cooperative Agreement No. DMR-2128556 and the State of Florida. CW-EPR measurements were performed with the support of the NSF-MRI

Program grant CHE-2320338. A portion of this research used resources of the National Energy Research Scientific Computing Center (NERSC), a Department of Energy Office of Science User Facility using NERSC award BES-ERCAP0032806. This work made use of the EPIC facility (RRID: SCR_026361) of Northwestern University's NUANCE Center, which has received support from the SHyNE Resource (NSF ECCS-2025633), the IIN, and Northwestern's MRSEC program (NSF DMR-2308691).

REFERENCES

(1) Kobayashi, Y.; Hernandez, O. J.; Sakaguchi, T.; Yajima, T.; Roisnel, T.; Tsujimoto, Y.; Morita, M.; Noda, Y.; Mogami, Y.; Kitada, A.; et al. An oxyhydride of $BaTiO_3$ exhibiting hydride exchange and electronic conductivity. *Nat. Mater.* **2012**, *11* (6), 507−511.

(2) Yajima, T.; Kitada, A.; Kobayashi, Y.; Sakaguchi, T.; Bouilly, G.; Kasahara, S.; Terashima, T.; Takano, M.; Kageyama, H. Epitaxial thin films of $ATiO_{3-x}H_x$ (A = Ba, Sr, Ca) with metallic conductivity. *J. Am. Chem. Soc.* **2012**, *134* (21), 8782−8785.

(3) Gao, T.; Nian, L.; Jin, L.; Sun, H.; Zhang, T.; Yang, J.; Gu, Z.; Peng, L.; Nie, Y. Giant Switchable Persistent Photoconductivity in Soft Chemistry Reduced $SrTiO_3$. *Adv. Electron. Mater.* **2023**, *9* (7), No. 2300068, DOI: 10.1002/aelm.202300068.

(4) Granhed, E. J.; Lindman, A.; Eklöf-Österberg, C.; Karlsson, M.; Parker, S. F.; Wahnström, G. Band vs. polaron: vibrational motion and chemical expansion of hydride ions as signatures for the electronic character in oxyhydride barium titanate. *J. Mater. Chem. A* **2019**, *7* (27), 16211−16221.

(5) Palfey, W. R.; Hwang, S.; Goddard, W. A., III; Rossman, G. R. The spectroscopy of hydride in single crystals of $SrTiO_3$ perovskite. *Phys. Chem. Chem. Phys.* **2024**, *26* (39), 25439−25451.

(6) Aleksis, R.; Nedumkandathil, R.; Papawassiliou, W.; Carvalho, J. P.; Jaworski, A.; Haussermann, U.; Pell, A. J. Probing the electronic structure and hydride occupancy in barium titanium oxyhydride through DFT-assisted solid-state NMR. *Phys. Chem. Chem. Phys.* **2022**, *24* (46), 28164−28173.

(7) Nedumkandathil, R.; Jaworski, A.; Grins, J.; Bernin, D.; Karlsson, M.; Eklof-Osterberg, C.; Neagu, A.; Tai, C. W.; Pell, A. J.; Haussermann, U. Hydride Reduction of $BaTiO_3$ - Oxyhydride Versus O Vacancy Formation. *ACS Omega* **2018**, *3* (9), 11426−11438.

(8) He, X.; Nomoto, S.; Komatsu, T.; Katase, T.; Tadano, T.; Kitani, S.; Yoshida, H.; Yamamoto, T.; Mizoguchi, H.; Ide, K.; et al. Hydride Anion Substitution Boosts Thermoelectric Performance of Polycrystalline $SrTiO_3$ via Simultaneous Realization of Reduced Thermal Conductivity and High Electronic Conductivity. *Adv. Funct. Mater.* **2023**, *33* (28), No. 2213144, DOI: 10.1002/adfm.202213144.

(9) Eklöf-Österberg, C.; Mazzei, L.; Granhed, E. J.; Wahnström, G.; Nedumkandathil, R.; Häussermann, U.; Jaworski, A.; Pell, A. J.; Parker, S. F.; Jalarvo, N. H.; et al. The role of oxygen vacancies on the vibrational motions of hydride ions in the oxyhydride of barium titanate. *J. Mater. Chem. A* **2020**, *8* (13), 6360−6371.

(10) Katase, T.; Nomoto, S.; He, X.; Kitani, S.; Honda, T.; Hiramatsu, H.; Hosono, H.; Kamiya, T. Simultaneous Realization of Single-Crystal-Like Electron Transport and Strong Phonon Scattering in Polycrystalline $SrTiO_{3-x}H_x$. *ACS Appl. Electron. Mater.* **2024**, *6* (10), 7424−7429.

(11) Eklöf-Österberg, C.; Nedumkandathil, R.; Häussermann, U.; Jaworski, A.; Pell, A. J.; Tyagi, M.; Jalarvo, N. H.; Frick, B.; Faraone, A.; Karlsson, M. Dynamics of Hydride Ions in Metal Hydride-Reduced $BaTiO_3$ Samples Investigated with Quasielastic Neutron Scattering. *J. Phys. Chem. C* **2019**, *123* (4), 2019−2030.

(12) Lavén, R.; Fine, L.; Naumovska, E.; Guo, H.; Hassermann, U.; Jaworski, A.; Matsuura, M.; Koza, M. M.; Karlsson, M. Mechanism of Hydride-Ion Diffusion in the Oxyhydride of Barium Titanate. *J. Phys. Chem. C* **2025**, *129* (27), 12305−12311.

(13) Liu, X.; Bjørheim, T. S.; Vines, L.; Fjellvåg, Ø. S.; Granerød, C.; Prytz, Ø.; Yamamoto, T.; Kageyama, H.; Norby, T.; Haugsrud, R. Highly Correlated Hydride Ion Tracer Diffusion in $SrTiO_{3-x}H_x$ Oxyhydrides. *J. Am. Chem. Soc.* **2019**, *141* (11), 4653−4659.

(14) Sakaguchi, T.; Kobayashi, Y.; Yajima, T.; Ohkura, M.; Tassel, C.; Takeiri, F.; Mitsuoka, S.; Ohkubo, H.; Yamamoto, T.; Kim, Je.; et al. Oxyhydrides of $(Ca,Sr,Ba)TiO_3$ Perovskite Solid Solutions. *Inorg. Chem.* **2012**, *51* (21), 11371−11376.

(15) Yamamoto, T.; Kageyama, H. Hydride Reductions of Transition Metal Oxides. *Chem. Lett.* **2013**, *42* (9), 946−953.

(16) Kobayashi, Y.; Li, Z.; Hirai, K.; Tassel, C.; Loyer, F.; Ichikawa, N.; Abe, N.; Yamamoto, T.; Shimakawa, Y.; Yoshimura, K.; et al. Gas phase contributions to topochemical hydride reduction reactions. *J. Solid State Chem.* **2013**, *207*, 190−193.

(17) Bowman, A.; Claridge, J. B.; Rosseinsky, M. J. Anion Composition Control and Magnetic Short- and Long-Range Order in Transition Metal Oxide Hydrides. *Chem. Mater.* **2006**, *18*, 3046−3056.

(18) Martelli, P.; Caputo, R.; Remhof, A.; Mauron, P.; Borgschulte, A.; Zuttel, A. Stability and Decompositon of $NaBH_4$. *J. Phys. Chem. C* **2010**, *114*, 7173−7177.

(19) Tan, H.; Zhao, Z.; Zhu, W.-b.; Coker, E. N.; Li, B.; Zheng, M.; Yu, W.; Fan, H.; Sun, Z. Oxygen Vacancy Enhanced Photocatalytic Activity of Pervoskite $SrTiO_3$. *ACS Appl. Mater. Interfaces* **2014**, *6* (21), 19184−19190.

(20) Toby, B. H.; Von Dreele, R. B. GSAS-II: the genesis of a modern open-source all purpose crystallography software package. *J. Appl. Crystallogr.* **2013**, *46* (2), 544−549.

(21) Massiot, D.; Fayon, F.; Capron, M.; King, I.; Le Calvé, S.; Alonso, B.; Durand, J. O.; Bujoli, B.; Gan, Z.; Hoatson, G. Modelling one- and two-dimensional solid-state NMR spectra. *Magn. Reson. Chem.* **2002**, *40* (1), 70−76.

(22) van Meerten, S. G. J.; Franssen, W. M. J.; Kentgens, A. P. M. ssNake: A cross-platform open-source NMR data processing and fitting application. *J. Magn. Reson.* **2019**, *301*, 56−66.

(23) Kresse, G.; Furthmuller, J. Efficiency of ab-initio total energy calculations for metals and semiconductors using a plane-wave basis set. *Comput. Mater. Sci.* **1996**, *6*, 15−50.

(24) Kresse, G.; Furthmuller, J. Efficient iterative schemes for ab initio total-energy calculations using a plane-wave basis set. *Phys. Rev. B* **1996**, *54*, 11169−11186.

(25) Kresse, G.; Hafner, J. Ab initio molecular dynamics for liquid metals. *Phys. Rev. B* **1993**, *47* (1), 558−561.

(26) Kresse, G.; Joubert, D. From ultrasoft pseudopotentials to the projector augmented-wave method. *Phys. Rev. B* **1999**, *59*, 1758−1775.

(27) Blöchl, P. E. Projector augmented-wave method. *Phys. Rev. B* **1994**, *50* (24), 17953−17979.

(28) Varley, J. B.; Janotti, A.; Van de Walle, C. G. Hydrogenated vacancies and hidden hydrogen in $SrTiO_3$. *Phys. Rev. B* **2014**, *89* (7), No. 075202, DOI: 10.1103/PhysRevB.89.075202.

(29) Kröger, F.; Vink, V. Relations between the Concentrations of Imperfections in Crystalline Solids. In *Solid State Physics*; Elsevier, 1956; Vol. *3*, pp 307−435.

(30) Becerra-Toledo, A. E.; Enterkin, J. A.; Kienzle, D. M.; Marks, L. D. Water adsorption on $SrTiO_3(001)$: II. Water, water, everywhere. *Surf. Sci.* **2012**, *606* (9−10), 791−802.

(31) Giannozzi, P.; Andreussi, O.; Brumme, T.; Bunau, O.; Buongiorno Nardelli, M.; Calandra, M.; Car, R.; Cavazzoni, C.; Ceresoli, D.; Cococcioni, M.; et al. Advanced capabilities for materials modelling with Quantum ESPRESSO. *J. Phys.: Condens. Matter* **2017**, *29* (46), No. 465901.

(32) Giannozzi, P.; Baroni, S.; Bonini, N.; Calandra, M.; Car, R.; Cavazzoni, C.; Ceresoli, D.; Chiarotti, G. L.; Cococcioni, M.; Dabo, I.; et al. QUANTUM ESPRESSO: a modular and open-source software project for quantum simulations of materials. *J. Phys.: Condens. Matter* **2009**, *21* (39), No. 395502.

(33) Ceresoli, D. Pseudopotentials 2025; https://sites.google.com/site/dceresoli/pseudopotentials?authuser=0. (accessed 2025).

(34) Dal Corso, A. Pseudopotentials periodic table: From H to Pu. *Comput. Mater. Sci.* **2014**, *95*, 337−350.

(35) Knight, W. D. Nuclear Magnetic Resonance Shift in Metals. *Phys. Rev.* **1949**, *76* (8), 1259−1260.
(36) Pyykkö, P. Year-2008 nuclear quadrupole moments. *Mol. Phys.* **2008**, *106* (16−18), 1965−1974.
(37) Reusch, W. *Nuclear Magnetic Resonance Spectroscopy*; Libretexts, 2023.
(38) Maekawa, H.; Kashii, N.; Kawamura, J.-I.; Hinatsu, Y.; Yamamura, T. High temperature H NMR study of proton conducting oxide $SrCe_{0.95}Y_{0.05}H_{0.004}O_{3-d}$. *Solid State Ionics* **1999**, *122*, 231−236.
(39) Tong, Y.; Rice, C.; Godbout, N.; Wieckowski, A.; Oldfield, E. Correlation between the Knight Shift of Chemisorbed CO and the Fermi Level Local Density of States at Clean Platinum Catalyst Surfaces. *J. Am. Chem. Soc.* **1999**, *121*, 2996−3003.
(40) Kobayashi, Y.; Tang, Y.; Kageyama, T.; Yamashita, H.; Masuda, N.; Hosokawa, S.; Kageyama, H. Titanium-Based Hydrides as Heterogeneous Catalysts for Ammonia Synthesis. *J. Am. Chem. Soc.* **2017**, *139* (50), 18240−18246.
(41) Kim, H.; Zhang, J. Y.; Raghavan, S.; Stemmer, S. Direct Observation of Sr Vacancies in $SrTiO_3$ by Quantitative Scanning Transmission Electron Microscopy. *Phys. Rev. X* **2016**, *6* (4), No. 041063, DOI: 10.1103/PhysRevX.6.041063.
(42) Hinojosa, B. B.; Van Cleve, T.; Asthagiri, A. A first-principles study of H_2O adsorption and dissociation on the $SrTiO_3$(100) surface. *Mol. Simul.* **2010**, *36* (7−8), 604−617.
(43) Bennett, L. H.; Watson, R. E.; Carter, G. C. Relevance of Knight Shift Measurments to the Electronic Density of States. *J. Res. Natl. Bur. Stand. A Phys. Chem.* **1970**, *74A*, 569−610, DOI: 10.6028/jres.074A.048.
(44) Misaki, T.; Oikawa, I.; Takamura, H. Negative Knight Shift in Ba-Ti Oxyhydride: An Indication of the Multiple Hydrogen Occupation. *Chem. Mater.* **2019**, *31* (18), 7178−7185.
(45) Korringa, J. Nuclear Magnetic Relaxation and Resonance Line Shift in Metals. *Physica* **1950**, *16*, 601−610.
(46) Zheng, W.-C.; Wu, X.-X. Studies of EPR g factors of the isoelectronic $3d^3$ series Cr^{3+}, Mn^{4+} and Fe^{5+} in $SrTiO_3$ crystals. *J. Phys. Chem. Solids* **2005**, *66* (10), 1701−1704.
(47) Zheng, W. C.; Wu, X. X. Studies of the EPR g factor for Ni2+ ion in CsMgX3 (X = Cl, Br, I) crystals. *Spectrochim. Acta, Part A* **2006**, *64* (3), 628−630.
(48) Lombard, P.; Ollier, N.; Boizot, B. EPR study of Ti3+ ions formed under beta irradiation in silicate glasses. *J. Non-Cryst. Solids* **2011**, *357* (7), 1685−1689.
(49) Xiao, Y.; Chen, S.; Wang, Y.; Hu, Z.; Zhao, H.; Xie, W. Ethanol-Quenching Introduced Oxygen Vacancies in Strontium Titanate Surface and the Enhanced Photocatalytic Activity. *Nanomaterials* **2019**, *9* (6), No. 883, DOI: 10.3390/nano9060883.
(50) Ran, X.; Bai, Y.; Zeng, H.; Zhang, J.; Fu, H.; An, X.; Yang, X. Manipulating Oxygen Vacancy in $SrTiO_3$ Nanoparticles to Achieve Enhanced Photoelectrochemical Performance in Water Splitting. *ACS Appl. Nano Mater.* **2024**, *7* (23), 27543−27554.
(51) Souto-Casares, J.; Spaldin, N. A.; Ederer, C. Oxygen vacancies in strontium titanate: A DFT+DMFT study. *Phys. Rev. Res.* **2021**, *3* (2), No. 023027, DOI: 10.1103/PhysRevResearch.3.023027.
(52) Janotti, A.; Varley, J. B.; Choi, M.; Van de Walle, C. G. Vacancies and small polarons in $SrTiO_3$. *Phys. Rev. B* **2014**, *90* (8), No. 085202, DOI: 10.1103/PhysRevB.90.085202.
(53) Wang, J.; Yu, Y.; Abdelkawy, A.; Li, J.; Li, J.; Yang, J.; Ko, E. K.; Lee, Y.; Thampy, V.; Cui, Y.; et al. Molecular H_2 as the Reducing Agent in Low-Temperature Oxide Reduction Using Calcium Hydride. *J. Am. Chem. Soc.* **2025**, *147* (4), 3032−3038.
(54) Sun, W.; Holder, A.; Orvañanos, B.; Arca, E.; Zakutayev, A.; Lany, S.; Ceder, G. Thermodynamic Routes to Novel Metastable Nitrogen-Rich Nitrides. *Chem. Mater.* **2017**, *29* (16), 6936−6946.
(55) NIST Chemistry Webbook. (accessed July 28, 2025).
(56) Kirklin, S.; Saal, J. E.; Meredig, B.; Thompson, A.; Doak, J. W.; Aykol, M.; Rühl, S.; Wolverton, C. The Open Quantum Materials Database (OQMD): assessing the accuracy of DFT formation energies. *npj Comput. Mater.* **2015**, *1*, No. 15010, DOI: 10.1038/npjcompumats.2015.10.
(57) Saal, J. E.; Kirklin, S.; Aykol, M.; Meredig, B.; Wolverton, C. Materials Design and Discovery with High-Throughput Density Functional Theory: The Open Quantum Materials Database (OQMD). *JOM* **2013**, *65* (11), 1501−1509.
(58) *The Merck Index*; Merck Co., Inc.: Rahway, NJ, 1983; Vol. *10*, p 1236.
(59) Gawley, R. E.; Hennings, D. D. Sodium Hydride. In *Encyclopedia of Reagents for Organic Synthesis*; Wiley, 2001.

https://doi.org/10.1021/acs.chemmater.5c03181
Chem. Mater. 2026, 38, 4961−4974